NaTi2(PO4)3 hollow nanoparticles encapsulated in carbon nanofibers as novel anodes for flexible aqueous rechargeable sodium-ion batteries

Bing He, Kuibo Yin, Wenbin Gong, Yuwei Xiong, Qichong Zhang, Jiao Yang, Zhixun Wang, Zhe Wang, Mengxiao Chen, Ping Man, et al.

$NaTi_2(PO_4)_3$ Hollow Nanoparticles Encapsulated in Carbon Nanofibers as Novel Anodes for Flexible Aqueous Rechargeable Sodium-Ion Batteries

Bing He[a,b+], Kuibo Yin[b+], Wenbin Gong[e+], Yuwei Xiong[b], Qichong Zhang[a, b, c*], Jiao Yang[a, c], Zhixun Wang[a], Zhe Wang[a], Mengxiao Chen[a], Ping Man[f], Philippe Coquet[c], Yagang Yao[d, g*], Litao Sun[b*] and Lei Wei[a,c*]

a. School of Electrical and Electronic Engineering, Nanyang Technological University, 50 Nanyang Avenue, 639798, Singapore

b. SEU-FEI Nano-Pico Center, Key Laboratory of MEMS of Ministry of Education, Southeast University, Nanjing, 210096, China.

c. CINTRA CNRS/NTU/THALES, UMI 3288, Research Techno Plaza, 50 Nanyang Drive, 637553, Singapore

d. National Laboratory of Solid State Microstructures, College of Engineering and Applied Sciences, and Collaborative Innovation Center of Advanced Microstructures, Nanjing University, Nanjing 210093, China

e. School of Physics and Energy, Xuzhou University of Technology, Xuzhou 221018, China

f. Department of Chemistry, City University of Hong Kong, Hong Kong, China

g. Division of Nanomaterials, Suzhou Institute of Nano-Tech and Nano-Bionics, Nanchang, Chinese Academy of Sciences, Nanchang, 330200, China

[*] Email: zhangqc@ntu.edu.sg, ygyao2018@nju.edu.cn, slt@seu.edu.cn, wei.lei@ntu.edu.sg

[+] These authors contribute equally to this work.

Abstract

NASICON-structured $NaTi_2(PO_4)_3$ (NTP) is an attractive anode material for aqueous rechargeable sodium-ion batteries (ARSIBs) thanks to its three-dimensional open framework and appropriate negative voltage window. Nevertheless, the lack of flexible and high-performance binder-free NTP-based anodes remains stumbling blocks to the development of wearable ARSIBs. Herein, hollow-structure NTP evenly encapsulated in cross-linked porous N-doped carbon nanofiber (HNTP@PNC) is prepared through electrospinning technology and subsequent carbonization treatment, directly acting as binder-free anode for flexible ARSIBs. Benefiting from its unique hollow structure, continuous conductive network and favorable synergistic effect, the HNTP@PNC electrode displays as high as of 108.3 mAh g^{-1} rate capacity at 5.50 A g^{-1} and an impressive cycling stability of 97.2% capacity retention after 3000 cycles. Further, theoretical calculations reveal that NTP with NC coating significantly enhances electronic conductivity and accelerates Na^+ diffusion kinetics. Pairing with potassium zinc hexacyanoferrate free-standing cathode, a prototype quasi-solid-state ARSIB with a high-voltage discharge plateau of 1.6 V is successfully constructed, achieving a high volumetric capacity of 24.5 mAh cm^{-3} and an admirable energy density of 39.2 mWh cm^{-3}, outperforming most reported flexible aqueous rechargeable energy-storage devices. These exciting results provide valuable intuition into the design of novel binder-free NTP-based anodes for next-generation wearable ARSIBs.

Keywords: $NaTi_2(PO_4)_3$, hollow structure, electrospinning, binder-free anodes, aqueous sodium-ion batteries

Introduction

Ever-increasing demand for portable and wearable next-generation technology has greatly boosted the research interest in develpoing high efficiency storage devices with elevated safety and mechanical flexibility.[1-24] Recently, sodium-ion batteries (SIBs) have emerged as highly favorable substitutes to lithium-ion battery for large-scale energy storage applications owning to large availability of sodium reserves and the homogenous chemical and physical properties to lithium ions.[25-32] However, sluggish kinetics, caused by the poor ionic conductivity of the traditional organic electrolytes and large radius of Na^+, commenly leads to inferior rate performance and power densities, thus limiting their practical applications in wearable electronics. Encouragingly, the emergence of aqueous electrolytes provides opportunities to construct high-power density SIBs because of the higher ion conductivity (~1 S cm^{-1}) than that of organic electrolytes (~1-10 mS cm^{-1}).[33, 34] Moreover, aqueous electrolytes possesss inherent biocompatibility and excellent safety, avoiding the issues arisen from the flammability and toxicity of organic electrolytes, thus they are appropriate for powering wearable electronics. [35-40] Besides, aqueous rechargeable SIBs (ARSIBs) show better prospect than widely investigated supercapacitors and zinc-ion batteries because the former are restricted by their serious self-discharge and the latter are hampered by the dendritic growth of Zn metal anode.[21, 41] Nevertheless, to date, there are only few reports on constructing flexible electrodes for wearable aqueous rechargeable SIBs (ARSIBs).[42, 43] Therefore, it is imperative to design and prepare the binder-free electrodes with the rational architecture for high-performance flexible ARSIBs.

Among various anode materials for ARSIBs, $NaTi_2(PO_4)_3$ (NTP), one known member of Na super ion conductor (NASICON) family with an open 3D framework, has been considered as

one of the most favourable anode materials for ARSIBs, due to its high ionic conductivity and suitable negative voltage platform.[44-50] Unfortunately, the inherent poor electronic conductivity and the difficulty in manufacturing flexible binder-free NTP-based anodes have severely restricted their application in flexible ARSIBs. Electrospinning and subsequent carbonization treatment are the effective way to prepare flexible binder-free electrodes for energy-storage devices.[51-60] More importantly, the construction of one dimensional (1D) carbon nanostructure not only facilitates the oriented and fast transmission of electronics and ions, but also accommodates the stress change caused by the intercalation and deintercalation of metal ions, especially for the ions with large ionic radius.[61, 62] Besides, the nanostructure design of active materials plays an important role in electrochemical performance. Hollow nanostructures have been widely adopted as an effective procedure to upgrade the physical and chemical properties of target materials in energy-storage research fields.[63-65] The electrode materials with hollow structures would possess numerous unique advantages, such as exposing large accessible specific surface area, reducing the distance of ion diffusion and accommodating the volumetric change during the procedure of charge and discharge, which could make contribution to the improvement of rate performance, specific capacity, and cycle stability.[66-68] However, the preparation of most electrode materials with hollow structures requires multiple steps or templates, resulting in complex processes and high costs.[69, 70] Thus, developing a facial and effective method remains a great challenge for constructing a flexible binder-free NTP-based electrode for FARSIBs with long-term cycling stability and high-rate capacity.

In this work, rugby-like NTP nanoparticles with hollow structures (HNTP) were synthesized by a modified mild solvothermal method, and then were uniformly embedded in

polyacrylonitrile (PAN) polymer fibers via electrospinning technique, followed by carbonization treatment, which led to the encapsulation of HNTP nanoparticles within porous N-doped carbon nanofiber (HNTP@PNC). Contributed by the continuous conductive networks composed of interlaced 1D carbon nanofibers and the unique hollow structure, the resulting HNTP@PNC film electrode delivered outstanding rate performance (87.1% at 5.50 A g^{-1}) and specific capacity (124.4 mAh g^{-1} at 0.275 A g^{-1}) as well as cycle stability (97.2% of initial capacity after 3000 cycles). Coupling with potassium zinc hexacyanoferrate arrays expanded on the surface of carbon nanotube films (CNTF@KZHCF) cathode, a flexible quasi-solid-state ARSIB was successfully gathered by employing HNTP@PNC film and CNTF@KZHCF as the binder-free anode and cathode. Encouragingly, the resulting ARSIB displayed offered prominent electrochemical performance and excellent mechanical flexibility. This work provides instructive material engineering for rational construction of binder-free NTP-based anodes aiming at wearable aqueous sodium-ion storage.

Experimental Section

Synthesis of rugby-like HNTP.

Solvothermal method that is a simple one-step method was used for synthesis of rugby-like HNTP. Generally, 1 mL $TiCl_3$ solution containing 30%wt of HCl was added into 30 mL mixed solution (volume ratio of ethylene glycol and ethanol is 1:1) by drop and drop under continuous stirring. In the same way, 1 mL H_3PO_4 was added into the above solution after mixing for 30 min. Then, put 1 g $NaH_2PO_4 \cdot 2H_2O$ into the mixed solution and stir for 30 min. Next, the as-prepared reaction solution was placed into a 50-mL reaction vessel and kept at 150 ^oC for 6 h. After cool down to room temperature, the HNTP powders were collected by filtration and rinsed with ethanol and distilled water. Finally, the acquired powers were dried at 60 ^oC for 24 h. Besides,

the NTP with solid structure was prepared with same conditions except for the reaction solution, in which the reaction solution is 30 mL ethylene glycol without ethanol.

Synthesis of HNTP@PNC.

0.2 g of the as-prepared HNTP power was placed into 2.5 g dimethylformamide (DMF) solvent and then sonicated and stirred for 3 h, followed by addition of 0.4 g Polyacrylonitrile (PAN, Mw=150,000 g mol^{-1}). After stirring for 24 h, the as-obtained solution was converted to a homogeneous white suspension. Then, a 2.5 mL syringe fitted out with a 21 gauge-steel blunt tip needle was filled with the precursor suspension. The injection speed and applied voltage were 1.0 mL h^{-1} and 15 kV, respectively. Additionally, the collection device is a cylindrical drum with a diameter of 10 cm and the rotate speed was 2000 rpm. The as-spun HNTP@PAN film was dried at 80 ^{o}C under vacuum for 24 h and subsequently stabilized under air atmosphere at 250 ^{o}C for 3 h. Finally, the stable HNTP@PAN film was carbonized by a stepwise calcination method (kept at 450 ^{o}C and at 800 ^{o}C for 2 h) with a ramping rate of 1 ^{o}C min^{-1} under Ar atmosphere to obtained flexible HNTP@PNC film and then the obtained film and CNTF were pressed together by a hot-pressing treatment for 3 h for the electrochemical tests as a flexible binder-free electrode (HNTP@PNC). For comparison, SNTP nanoparticles were prepared by same method to obtain a binder-free film electrode.

Results and Discussion

As shown in Fig. 1a, NASICON-type structured NTP is consisted of TiO_6 octahedrons and PO_4 tetrahedrons, which are connected to each other through oxygen atoms. A facial and mild solvothermal method was employed to synthesized rugby-like solid NTP (SNTP) (Fig. S1). To achieve better physical and chemical properties, rugby-like hollow NTP (HNTP) was prepared via altering the reaction solvent. The images of transmission electron microscopy (TEM) and

scanning electron microscopy (SEM) show uniformly distributed HNTP nanoparticles with an average size of 400 nm (Figs. 1b and 1c). For HNTP particles, the thickness of shell is about 15 nm as verified in TEM image (Fig. S2). Besides, elemental mapping images of energy-dispersive X-ray (EDX), shown in Fig. 1d, illustrate the homogeneous placement of elements like Na, Ti, P, and O, which further confirm the hollow structure. Moreover, the energy dispersive spectroscopy (EDS) results, shown in Fig. 1e, clearly demonstrate that the atomic ratios of elements O: P: Ti: Na is about 12: 3: 2: 1. These results are in good agreement with the molecular formula of NTP. From the high-resolution TEM image (Fig. 1f), the clear lattice fringes with an interplanar placing of 0.365 nm correspond to the (113) plane of the NTP. Furthermore, the pattern of Selected Area Electron Diffraction (SAED) (Fig. 1g) shows bright diffraction spots, implying high crystal nature of HNTP. The crystal structures of solid NTP and HNTP were also analyzed by XRD pattern in Fig. 1h. It is worth to emphasize that all diffraction peaks of SNTP and HNTP are almost identical and coincide with the $NaTi_2(PO_4)_3$ (JCPDS card No. 33–1296), which suggests that the transformation of NTP from solid structure to hollow structure makes no influence on the structural composition of the material. Measurements for N_2 adsorption-desorption were carried out in order to investigate the change of surface area of solid and hollow structure, as shown in Fig. 1i. The surface areas of SNTP and HNTP are 38.8 and 64.7 $m^2 g^{-1}$, revealing that the design of hollow structure enlarges the surface area of active materials. The HNTP with large surface area is beneficial to achieve more abundant active reactive sites, faster ion diffusion and more stable electrochemical performance.

To investigate the formation mechanism of hollow structure, we have performed TEM characterization on samples obtained at different solvothermal reaction times. As shown in Fig. S3b, the powder obtained after reaction for 1 h exhibits solid rugby-like structure with an

average size of 250 nm. After reacting for another hour, the particle size has been further increased and the core-shell structure phenomenon has begun to appear (Fig. S3c). As the reaction time increases, the volume of core gradually decreases (Fig. S3d). Upon prolonging reaction time to 6 h, the core disappears and the core-shell structure transfers to hollow structure, as shown in Fig. S3e. Based on the above results, a possible mechanism for the formation of rugby-like NTP with hollow structure has been illustrated in Fig. S3a, which may be attributed to an Ostwald ripening process. Interestingly, in the case of a single reaction solvent (ethanol or ethylene glycol), the Ostwald ripening phenomenon would not occur as reaction time increases, accordingly not forming the hollow structure, as shown in Figs. S1 and S4. Therefore, the mixture of ethanol and ethylene glycol could promote the process of dissolution and recrystallization, becoming the key factor in forming a hollow structure.

To prepare flexible binder-free electrodes, the fabrication procedure with electrospun and subsequent annealing treatment is schematically shown in Fig. 2a. Firstly, the as-obtained rugby-like HNTP nanoparticles were dispersed in a polyacrylonitrile/dimethylformamide (PAN/DMF) solution with vigorous stirring to form a homogeneous electrospun solution. Subsequently, the voltage between needle and drum was 15 KV and injection speed was 1 mL h^{-1}. Finally, the obtained HNTP@PAN nanofiber hybrid film (Fig. S5) was annealed at 250 ^{o}C at air atmosphere and further carbonized at 800 ^{o}C in Ar atmosphere to obtained HNTP@PNC nanofibers. During the PAN carbonization, nitrogen doping and porous structure of the carbon nanofibers were presented due to the releasing gases and N-rich character of PAN. As revealed by SEM images (Figs. 2b and S6), the obtained HNTP@PNC hallmark a reticular shape interlinked by rough nanofibers. Compared with the PNC nanofibers without adding HNTP nanoparticles (Fig. S7), the rough surface of the HNTP@PNC sample elucidates that the HNTP nanoparticles were

tightly encapsulated by the carbon nanofibers (Figs. 2c and 2d). As elucidated by high-resolution TEM image (Fig. 2e), the surface of HNTP is uniformly covered with a thin layer of amorphous carbon. Fig. 2f displays EDS element mappings of the HNTP@PNC nanofiber, verifying an even distribution of elements (O, Na, P and Ti,) along the entire framework of fibrous N-doped carbon. A flexible binder-free film electrode using SNTP as active material, denoted as SNTP@PNC, was assembled by the same technique for the purpose of comparison. It is clearly seen from the SEM image in Fig. S8 that the SNTP is evenly distributed in the porous N-doped carbon nanofibers.

The crystal structure and chemical composition of the obtained HNTP@PNC film were characterized by XRD, Raman, and XPS (X-ray photoelectron spectroscopy), as presented in Fig. 3. XRD pattern of HNTP@PNC film is shown in Fig. 3a, in which all the diffraction peaks are indexed to the $NaTi_2(PO_4)_3$ (JCPDS card No. 33-1296), except for the broad characteristic peak of PNC. Raman spectrum of HNTP@PNC film (Fig. 3b) exhibits the apparent D and G bands, implying the existence of disordered amorphous carbon and crystalline graphic carbon. The higher relative intensity of D band reveals the amorphous features of carbon nanofiber, which is coincided with the result of high-resolution TEM. Besides, the weight percentage of NC could be analyzed via the weight loss from the thermogravimetric measurement in Fig. 3c, where a weight loss of 32.1 wt% is the NC content. The full XPS spectrum in Fig. S9 displays the signals of Na, Ti, P, O, C, and N, which strongly complies with the result of elemental mapping. The peak at 1072.2 eV is corresponding to the Na 1s (Fig. 3d). For the spectrum of Ti 2p, two main peaks located at 460.1 eV and 466.0 eV, can be allocated to the $2p_{3/2}$ and $2p_{1/2}$ components of Ti^{4+}, while two other peaks at 458.3 eV and 464.6 eV correspond to the lower titanium oxidation states of Ti^{3+} (Fig. 3e), implying the valence state of Ti is mainly +4. The XPS spectrum (Fig. 3f)

of P 2p can be assigned to two peaks of $2p_{1/2}$ (134.5 eV) and $2p_{3/2}$ (133.6 eV). Fig. 3g exhibits the high-solution O 1s spectrum, in which the fitted peaks locate at 531.5 eV, 532.6 eV and 533.2 eV. The peak at binding energy of 531.5 eV can be ascribed to the Na-O-P, Ti-O-P, and P=O, while the peaks at 532.6 eV and 533.2 eV correspond to P-O-H and C-O, respectively. As shown in Fig. 3h, the spectrum of C 1s could be divided into three peaks of C-C (284.7 eV), C-O (286.0 eV), and O-C=O (288.3 eV). The XPS spectrum of N 1s (Fig. 3i) distinctly demonstrates the existence of pyrrolic-N, pyridinic-N, and pyridine-N-oxide, further confirming the successful preparation of NC.

The electrochemical properties of the binder-free HNTP@PNC film electrode were examined in a three-electrode system using 1 M $NaClO_4$ as the aqueous electrolyte. Fig. 4a shows the comparison CV curves of HNTP@PNC and PNC film electrodes at a scan rate of 5 mV s^{-1}. In contrast to the PNC electrode, the HNTP@PNC electrode with the same length displays much larger CV area, implying that PNC makes very little contribution to the capacity of HNTP@PNC electrode. The electrochemical performance of HNTP@PNC and SNTP@PNC electrodes was further estimated by galvanostatic charge-discharge (GCD) curves at a current density of 1.10 A g^{-1} in Fig. 4b, both of which depict obvious charge/discharge plateaus, corresponding to the equilibrium voltage of Ti^{4+}/Ti^{3+}. Moreover, HNTP@PNC electrode has longer discharge plateau and lower voltage hysteresis compared with SNTP@PNC electrode, suggesting that HNTP@PNC delivers higher capacity and faster kinetics. The improvement of kinetics is further demonstrated by electrochemical impedance spectroscopy (EIS) measurements. As illustrated in Fig. 4c, HNTP@PNC electrode possesses greater slope than that of SNTP@PNC electrode in the low frequency region, which further implies a faster diffusion and transport of Na^+ during process of charge-discharge. All the CV curves in Fig. 4d clearly

illustrate symmetrical redox peaks and maintain the same shape at different scan rates, indicating highly reversible electrochemical reaction. Besides, the corresponding b values (slope values) of peak 1 and 2 are calculated to be 0.59 and 0.73 (Fig. 4e), revealing a process combined with surface-controlled and diffusion-controlled.[71-75] Fig. 4f depicts the GCD curves of the HNTP@PNC electrode at different current densities from 0.275 A g^{-1} to 5.50 A g^{-1}, which possess a stable discharge plateaus at -0.65 to -0.80 V. Notably, the HNTP@PNC electrode could deliver higher specific capacity of 124.4 mAh g^{-1} at a current density of 0.275 A g^{-1} and capacity retention of 87.1% of initial capacity at 5.50 A g^{-1} (Fig. 4g), whereas the NTP@PNC electrode only achieves a relatively low capacity (100.2 mAh g^{-1}) and 63.6% capacity retention, indicating that the design of hollow structure is conducive to the improvement rate performance and specific capacity. More importantly, the HNTP@PNC exhibits excellent electrochemical stability with 97.2% of the initial capacity after 3000 cycles at a current density of 5.50 A g^{-1}. In addition, the SEM, TEM, and XRD measurements were carried out to investigate the morphological and structural evolutions of HNTP@PNC after cycle test, as shown in Figs. S10 and S11. By contrast, the SNTP@PNC only maintains 80.1% of initial capacity after 3000 cycles. These inspiring results of HNTP@PNC electrode might be attributed to the different reasons which are discussed here. Firstly, the design of hollow structure with the functional thin shells and the inner voids can lead to an increase in specific surface area accessible to the electrolyte, accordingly delivering higher specific capacity than the solid structure. Besides, the hollow structure and binder-free electrode shorten ion diffusion length and form a continuous conductive network, whose combination can facilitate the fast diffusion and transport of ions and electronics, further improving the rate performance. Moreover, the rational design of HNTP@PNC could

accommodate the volumetric change of electrode materials during the ion insertion and extraction, especially for Na^+ with large ionic radius, thereby achieving excellent cycle stability.

To clearly reveal the storage mechanism of NTP-based electrode, ex-situ XPS measurement was carried out to explore the valence states of Ti under different charge-discharge states. As shown in Fig. S12, when the NTP-based electrode is at 0 V or initial state, the peaks of Ti 2p mainly located 460.1 and 466.0 eV, which corresponds to Ti^{4+}. When charged to -1.2 V, the location of main peak (Ti $2p_{3/2}$) shifts to 458.3 eV, implying that Ti^{4+} is reduced to Ti^{3+} with the insertion of Na^+. During the subsequent discharging process, the peaks of Ti 2p return to the initial position, which indicates that the Ti^{3+} is oxidized to Ti^{4+}, meanwhile demonstrating high reversibility of the electrochemical reaction. Based on above analysis, the reaction equation of the anode is as follow:

$$NaTi_2(PO_4)_3 + 2\ Na+ + 2\ e- \rightleftharpoons Na_3Ti_2(PO_4)_3$$

Density functional theory (DFT) simulation was performed to explore the mechanisms of the Na ion storage in NTP@NC. Generally, the NxTP primitive cell for x = 1, 2, 3 and 4 consists of an open framework of corner sharing PO_4 tetrahedra and TiO_6 octahedra with two different sites available for occupation of Na. These sites are M1 (Wyckoff: 6b (0, 0, 0)) and M2 (Wyckoff: 18e (x, 0, 1/4)) (as shown in the inset). At low sodium content (x = 1), Na ions occupy the M1 site, while the intercalated Na ions at high sodium content (x > 1) occupy the M2 site. In this study, a layer of NC sheet placed on the (011) surface of the NTP primitive cell was employed to model the NTP@NC interface structure. It is found that the distance between NTP and NC at the NTP@NC interface as shown in Fig. 5a and 5b, is around 3.0 Å, suggesting the physical interaction between the NTP and NC. The calculated density of sates of NTP and NTP@NC in

Fig. 5c clearly shows a significant shift from the valence band towards the conductive region upon the addition of the N-doped carbon with NTP, which illustrates that NTP@NC has become greatly metallic in nature, and thus, consequently becomes conductive, which is beneficial to the performances of the battery. To investigate the Na storage abilities of NTP, the formation energies of Na ion intercalation into NTP were calculated and illustrated in Fig. 5d. It is found that the Na ions prefer to intercalate into NTP, since the formation energy keeps decreasing until 4 additional Na ions intercalate into an NTP primitive cell, in which there are 2 original Na ions to form N3TP. The slightly increased formation energy of N4TP compared with N3TP suggests that it is not easy to form the N4TP in reality, which consists quite well with our experimental observations. To further investigate the ion conductivity of NTP@NC, the ionic diffusions were considered. The Na ion diffusion through NC was firstly calculated as shown in Fig. 5e. It is clearly found that although the diffusion barrier through NC with a single vacancy is as high as 4.64 eV, two/three vacancies dramatically reduce the barriers to only 1.39/0.91 eV. Actually, multiple vacancies have been found to be thermodynamically favored over the single vacancy in the carbon sheets, guaranteeing the easy passing of Na ions through NC to be stored in NTP. In order to investigate the Na ion mobility in NTP and NTP@NC which dramatically determines the charging/discharging rate of the battery, the Na ion diffusion paths and the corresponding barriers for the NTP bulk and NTP@NC interface were calculated through the nudge elastic band (NEB) method as shown in Figs. 5f and S13. The M1 and M2 sites of NxTP provide three diffusion paths for Na ions, which are Na_{M1} to Na_{M2} (path1), Na_{M2} to Na_{M1} (path2) and Na_{M2} to Na_{M2} (path3), where Na_{M1} and Na_{M2} present the Na ions located in M1 and M2 sites. It is found that the diffusion barriers between adjacent M1 and M2 sites (path1 and path2) are relatively small (0.5 ~ 0.6 eV), while the diffusion barriers between adjacent M2 sites (path3) are higher

(1.8 eV) in bulk NTP. Strikingly, the diffusion barrier along path3 pronouncedly decreases by 1.0 eV at the interface of NTP@NC, while the diffusion barriers along path1 and path2 almost remain unchanged (0.6 ~ 0.7 eV). This ion diffusion property in NTP@NC is instrumental in the electrochemical kinetics for Na ion storage, since the ions can quickly spread at the NTP@NC interface along all the three diffusion paths, and then intercalate into the NTP along path1 and path2.

Prussian blue analogs have been widely investigated as cathode materials for alkali metal ion batteries.[76-78] Recently, we developed a facial and mild method to grow cube-like KZHCF on carbon cloth as the binder-free cathode for wearable ARSIBs, exhibiting excellent electrochemical performance and mechanical flexibility.[79] In this study, KZHCF arrays were successfully prepared on light and highly conductive carbon nanotube film (CNTF) as the cathode. Fig. S14 shows the SEM image of CNTF composed of intertwined CNTs, which is a promising flexible conductive substrate. Homogeneous and thin metal Zn nanosheets are grown on CNTF surface by a simple electrochemical deposition (Fig. S15). The XRD pattern (Fig. S16) exhibits that all diffraction peaks can be indexed to the standard hexagonal zinc (No. 87-0713). After subsequent redox process, the polyhedron-like KZHCF arrays are successfully synthesized using metal Zn nanosheets as the Zn source and reducing agent, as shown in Fig. S17. The TEM image (Fig. S18) further confirms the polyhedron-like structure with a size of ~1 μm. The crystal structure of the obtained CNTF@KZHCF is analyzed by the XRD pattern (Fig. S19), and all of the characteristic peaks can be well indexed to those of the standard $K_2Zn_3(Fe(CN)_6)_2 \cdot 9H_2O$ (JCPDS # 33-1061). Besides, the chemical composition of KZHCF is further confirmed by the XPS spectra (Fig. S20). The electrochemical performance of as-prepared CNTF@KZHCF was explored in a three-electrode system with 1 M $NaClO_4$ as aqueous electrolyte. Fig. S21a displays

the CV curves of CNT@KZHCF at different scan in 1-5 mV s^{-1} range with sharp and symmetry redox peaks. GCD curves of the as-prepared CNT@KZHCF cathode at various densities of current in 0.5-10 mA cm^{-2} range are presented in Fig. S21b, again exhibiting typical battery-like behavior. Remarkably, the CNT@KZHCF delivers a high capacity of 0.114 mAh cm^{-2} at 0.5 mA cm^{-2} and still retains 0.086 mAh cm^{-2} at 10 mA cm^{-2}.

As depicted in Fig. 6a, a flexible quasi-solid-state belt-like ARSIB is assembled with HNTP@PNC film and CNTF@KZHCF as the anode and cathode. The illustrations of the crystal structures of open-framework cathode and NASICON anode for as-assembled ARSIB are displayed in Fig. 6b, which are capable to achieve fast and reversibly insertion/extraction of Na^+. In addition, both these CV curves of the anode and cathode consist of a pair of strong redox peaks, which can be expected to construct a full cell with a high voltage (Fig. 6c). Consequently, a pair of typical redox peaks are observed at scan rate from 1 to 5 mV s^{-1} in the range of 0.6-1.9 V for each CV curve of the as-assembled ARSIB (Fig. 6d). To investigate the kinetics for Na^+ storage, the b values calculated from its CV curves are shown in Fig. S22. The b values, corresponding to peak 1 and 2, are 0.80 and 0.74, likewise belonging to a combination of surface-control and diffusion-control.[22] Evidently, the calculated capacitive contributions significantly increase from 50.3% to 71.0% with scan rates from 1 to 5 mV s^{-1} (Figs. 6e and 6f). Benefiting from the relatively high capacitive ratio, it is expected that our ARSIB has excellent rate performance. Fig. 6g shows the GCD curves of our device at different current densities with stable discharge plateaus between 1.4 and 1.6 V. Impressively, a high volumetric capacity of 24.5 mAh cm^{-3} is achieved at a current density of 0.04 A cm^{-3}, while 62.0% of the initial capacity can be still retained when the current density increased to 0.8 A cm^{-3}, displaying an outstanding rate capability. Besides, the specific capacity based on the total mass of anode and cathode active

materials is calculated to be about 32.3 mAh g^{-1} at 0.04 A cm^{-3}. Note that energy and power densities are extremely important parameters for energy storage device. The Ragone plots in Fig. 6h compare the volumetric energy and power densities of our ARSIB with other flexible aqueous energy-storage devices (FAESDs). More encouragingly, an admirable energy density of 39.2 mWh cm^{-3} at a power density of 64 mW cm^{-3} was achieved, which still retained an energy density of 21.0 mWh cm^{-3} at a high power density of 1104 mW cm^{-3} for our device, exceeding those of previously reported FAESDs, such as CNTs//Fe_3O_4-C battery-supercapacitor hybrid device [80], Ni//Fe battery [81], MnO_2//Fe_2O_3 supercapacitor [82], VO_x//VN supercapacitor [83], Co//Zn battery [84], Ni//Zn battery [85]. Concurrently, the mass energy and power densities of our device are exhibited in Fig. S23. As observed in Fig. S24, the as-assembled flexible ARSIB harvests an impressive capacity retention of 89.6% after 200 cycles with a maintenance of 100% Coulombic efficiency, revealing its remarkable long-cycle performance. Due to its flexible electrode materials and gel electrolyte as used, our ARSIB is expected to be highly flexible. The as-assembled ARSIB can be bent at different angles with negligible capacity decay (Fig. 6i), thereby implying its excellent mechanical stability. In addition, the bending stability of the device was tested as shown in Fig. S25, and only about 10.2% of initial capacity loss was observed after bending for 500 cycles at 90°. The output voltage and capacity are doubled when two flexible batteries are connected in series (Fig. S26a) or in parallel (Fig. S26b), respectively. As a demonstration of practical applications, two series-connected assembled devices can illuminate a blue LED (Fig. S27). Notably, two batteries still function well regardless of bending or squeezing.

Conclusion

In summary, through feasible electrospinning and thermal treatment processes, NTP nanoparticles with hollow structure were confined delicately in porous N-doped carbon nanofibers. When evaluated as flexible binder-free anode for ARSIB, the rationally designed NTP@PNC film took advantage of the fast ion diffusion, increased surface area, continuous conductive network and strong accommodation for stress change, yielding high specific capacity accompanied with prolonged cycle life and excellent rate capability. As evidenced by theoretical calculations, HNTP with NC coating dramatically facilitated the electrons and Na^+ ions diffusion kinetics. Furthermore, by adopting well-designed HNTP@PNC film electrode as anode and CNTF@KZHCF electrode as cathode, a flexible quasi-solid-state ARSIB was successfully assembled with high output voltage platform of 1.6 V, achieving high volumetric capacity (24.5 mAh cm^{-3}) and admirable energy density (39.2 mW h cm^{-3}). Thus, our work not only develops a new high-performance and flexible NTP-based anode material for wearable ARSIB, but also gives guidance on binder-free electrode designs for next-generation energy storage devices.

Acknowledgements

This work was supported by the Singapore Ministry of Education Academic Research Fund Tier 2 (MOE2019-T2-2-127 and T2EP50120-0005), A*STAR under AME IRG (A2083c0062), the Singapore Ministry of Education Academic Research Fund Tier 1 (RG90/19 and RG73/19) and the Singapore National Research Foundation Competitive Research Program (NRF-CRP18-2017-02). This work was also supported by Nanyang Technological University.

Notes and references

† Electronic supplementary information (ESI) available.

[1] K. Zhu, T. Wu, K. Huang, Adv. Energy Mater. 9 (2019) 1901968.

[2] Y. Zhao, Y. Zhang, H. Sun, X. Dong, J. Cao, L. Wang, Y. Xu, J. Ren, Y. Hwang, I. H. Son, X. Huang, Y. Wang, H. Peng, Angew. Chem. Int. Ed. 55 (2016) 14384-14388.

[3] Q. Zhang, W. Xu, J. Sun, Z. Pan, J. Zhao, X. Wang, J. Zhang, P. Man, J. Guo, Z. Zhou, B. He, Z. Zhang, Q. Li, Y. Zhang, L. Xu, Y. Yao, Nano Lett. 17 (2017) 7552-7560.

[4] Q. Zhang, C. Li, Q. Li, Z. Pan, J. Sun, Z. Zhou, B. He, P. Man, L. Xie, L. Kang, X. Wang, J. Yang, T. Zhang, P. P. Shum, Q. Li, Y. Yao, L. Wei, Nano Lett. 19 (2019) 4035-4042.

[5] N. Zhang, X. Chen, M. Yu, Z. Niu, F. Cheng, J. Chen, Chem. Soc. Rev. 49 (2020) 4203-4219.

[6] Y. Zeng, X. Zhang, Y. Meng, M. Yu, J. Yi, Y. Wu, X. Lu, Y. Tong, Adv. Mater. 29 (2017) 1700274.

[7] J. Yang, Q. Zhang, Z. Wang, Z. Wang, L. Kang, M. Qi, M. Chen, W. Liu, W. Gong, W. Lu, P. P. Shum, L. Wei, Adv. Energy Mater. 10 (2020) 2001064.

[8] T. Xiong, Y. Zhang, W. S. V. Lee, J. Xue, Adv. Energy Mater. 10 (2020) 2001769.

[9] C. Xia, J. Guo, Y. Lei, H. Liang, C. Zhao, H. N. Alshareef, Adv. Mater. 30 (2018) 1705580.

[10] X. Wu, Y. Xu, C. Zhang, D. P. Leonard, A. Markir, J. Lu, X. Ji, J. Am. Chem. Soc. 141 (2019) 6338-6344.

[11] F. Wan, Y. Zhang, L. Zhang, D. Liu, C. Wang, L. Song, Z. Niu, J. Chen, Angew. Chem. Int. Ed. 58 (2019) 7062-7067.

[12] F. Wan, S. Huang, H. Cao, Z. Niu, ACS Nano 14 (2020) 6752-6760.

[13] H. Qiu, X. Du, J. Zhao, Y. Wang, J. Ju, Z. Chen, Z. Hu, D. Yan, X. Zhou, G. Cui, Nat. Commun. 10 (2019) 5374.

[14] Z. Pan, J. Yang, J. Yang, Q. Zhang, H. Zhang, X. Li, Z. Kou, Y. Zhang, H. Chen, C. Yan, J. Wang, ACS Nano 14 (2020) 842-853.

[15] L. Ma, S. Chen, C. Long, X. Li, Y. Zhao, Z. Liu, Z. Huang, B. Dong, J. A. Zapien, C. Zhi, Adv. Energy Mater. 9 (2019) 1902446.

[16] Z. Liu, Q. Yang, D. Wang, G. Liang, Y. Zhu, F. Mo, Z. Huang, X. Li, L. Ma, T. Tang, Z. Lu, C. Zhi, Adv. Energy Mater. 9 (2019) 1902473.

[17] J. Liu, C. Guan, C. Zhou, Z. Fan, Q. Ke, G. Zhang, C. Liu, J. Wang, Adv. Mater. 28 (2016) 8732-8739.

[18] W. Li, K. Wang, S. Cheng, K. Jiang, Adv. Energy Mater. 9 (2019) 1900993.

[19] M. Li, Q. He, Z. Li, Q. Li, Y. Zhang, J. Meng, X. Liu, S. Li, B. Wu, L. Chen, Z. Liu, W. Luo, C. Han, L. Mai, Adv. Energy Mater. 9 (2019) 1901469.

[20] C. Li, Z. Sun, T. Yang, L. Yu, N. Wei, Z. Tian, J. Cai, J. Lv, Y. Shao, M. H. Rummeli, J. Sun, Z. Liu, Adv. Mater. 32 (2020) 2003425.

[21] M. S. Javed, H. Lei, Z. Wang, B.-t. Liu, X. Cai, W. Mai, Nano Energy 70 (2020) 104573.

[22] J. Hao, B. Li, X. Li, X. Zeng, S. Zhang, F. Yang, S. Liu, D. Li, C. Wu, Z. Guo, Adv. Mater. 32 (2020) 2003021.

[23] S. Guo, S. Liang, B. Zhang, G. Fang, D. Ma, J. Zhou, ACS Nano 13 (2019) 13456-13464.

[24] J. Ding, Z. Du, B. Li, L. Wang, S. Wang, Y. Gong, S. Yang, Adv. Mater. 31 (2019) 1904369.

[25] C. Xu, Y. Xu, C. Tang, Q. Wei, J. Meng, L. Huang, L. Zhou, G. Zhang, L. He, L. Mai, Nano Energy 28 (2016) 224-231.

[26] H. Xia, X. Zhu, J. Liu, Q. Liu, S. Lan, Q. Zhang, X. Liu, J. K. Seo, T. Chen, L. Gu, Y. S. Meng, Nat. Commun. 9 (2018) 5100.

[27] L. Shen, Y. Wang, F. Wu, I. Moudrakovski, P. A. van Aken, J. Maier, Y. Yu, Angew. Chem. Int. Ed. 58 (2019) 7238-7243.

[28] L. Shen, Y. Wang, H. Lv, S. Chen, P. A. van Aken, X. Wu, J. Maier, Y. Yu, Adv. Mater. 30 (2018) 1804378.

[29] P. K. Nayak, L. Yang, W. Brehm, P. Adelhelm, Angew. Chem. Int. Ed. 57 (2018) 102-120.

[30] Z. Li, Y. Fang, J. Zhang, X. W. D. Lou, Adv. Mater. 30 (2018) 1800525.

[31] W. Li, C. Han, W. Wang, Q. Xia, S. Chou, Q. Gu, B. Johannessen, H. Liu, S. Dou, Adv. Energy Mater. 10 (2019) 1903006.

[32] T. Jin, Q. Han, L. Jiao, Adv. Mater. 32 (2020) 1806304.

[33] X. Dong, L. Chen, J. Liu, S. Haller, Y. Wang, Y. Xia, Sci. Adv. 2 (2016) 1501038.

[34] G. Fang, J. Zhou, A. Pan, S. Liang, ACS Energy Lett. 3 (2018) 2480-2501.

[35] L. Suo, O. Borodin, Y. Wang, X. Rong, W. Sun, X. Fan, S. Xu, M. A. Schroeder, A. V. Cresce, F. Wang, C. Yang, Y.-S. Hu, K. Xu, C. Wang, Adv. Energy Mater. 7 (2017) 1701189.

[36] S. Qiu, X. Wu, M. Wang, M. Lucero, Y. Wang, J. Wang, Z. Yang, W. Xu, Q. Wang, M. Gu, J. Wen, Y. Huang, Z. J. Xu, Z. Feng, Nano Energy 64 (2019) 103941.

[37] R.-S. Kühnel, D. Reber, C. Battaglia, ACS Energy Lett. 2 (2017) 2005-2006.

[38] L. Jiang, L. Liu, J. Yue, Q. Zhang, A. Zhou, O. Borodin, L. Suo, H. Li, L. Chen, K. Xu, Y. S. Hu, Adv. Mater. 32 (2020) 1904427.

[39] J. Han, M. Zarrabeitia, A. Mariani, Z. Jusys, M. Hekmatfar, H. Zhang, D. Geiger, U. Kaiser, R. J. Behm, A. Varzi, S. Passerini, Nano Energy 77 (2020) 105176.

[40] D. Bin, F. Wang, A. G. Tamirat, L. Suo, Y. Wang, C. Wang, Y. Xia, Adv. Energy Mater. 8 (2018) 1703008.

[41] M.S. Javed, S.S.A. Shah, T. Najam, S.H. Siyal, S. Hussain, M. Saleem, Z. Zhao, W. Mai, Nano Energy 77 (2020) 105276.

[42] Q. Zhang, P. Man, B. He, C. Li, L. Qiulong, Z. Pan, Z. Wang, J. Yang, Z. Wang, Z. Zhou, X. Lu, Z. Niu, Y. Yao, L. Wei, Nano Energy 67 (2019) 104212.

[43] B. He, P. Man, Q. Zhang, H. Fu, Z. Zhou, C. Li, Q. Li, L. Wei, Y. Yao, Nano-Micro Lett. 11 (2019) 101.

[44] Q. Yang, S. Cui, Y. Ge, Z. Tang, Z. Liu, H. Li, N. Li, H. Zhang, J. Liang, C. Zhi, Nano Energy 50 (2018) 623-631.

[45] Y. Wang, L. Mu, J. Liu, Z. Yang, X. Yu, L. Gu, Y.-S. Hu, H. Li, X.-Q. Yang, L. Chen, X. Huang, Adv. Energy Mater. 5 (2015) 1501005.

[46] W. Ren, X. Chen, C. Zhao, Adv. Energy Mater. 8 (2018) 1801413.

[47] Z. Liu, Y. An, G. Pang, S. Dong, C. Xu, C. Mi, X. Zhang, Chem. Eng. J. 353 (2018) 814-823.

[48] C. Liu, X. Wang, W. Deng, C. Li, J. Chen, M. Xue, R. Li, F. Pan, Angew. Chem. Int. Ed. 57 (2018) 7046-7050.

[49] M. H. Lee, S. J. Kim, D. Chang, J. Kim, S. Moon, K. Oh, K.-Y. Park, W. M. Seong, H. Park, G. Kwon, B. Lee, K. Kang, Mater. Today 29 (2019) 26-36.

[50] Z. Guo, Y. Zhao, Y. Ding, X. Dong, L. Chen, J. Cao, C. Wang, Y. Xia, H. Peng, Y. Wang, Chem 3 (2017) 348-362.

[51] J. Yan, Y. Han, S. Xia, X. Wang, Y. Zhang, J. Yu, B. Ding, Adv. Funct. Mater. 29 (2019) 1907919.

[52] J. Yan, K. Dong, Y. Zhang, X. Wang, A. A. Aboalhassan, J. Yu, B. Ding, Nat. Commun. 10 (2019) 5584.

[53] J. Xue, T. Wu, Y. Dai, Y. Xia, Chem. Rev. 119 (2019) 5298-5415.

[54] S. Wang, R. Wang, Y. Bian, D. Jin, Y. Zhang, L. Zhang, Nano Energy 55 (2019) 173-181.

[55] X. Sun, C. Wang, Y. Gong, L. Gu, Q. Chen, Y. Yu, Small 14 (2018) 1802218.

[56] G. Song, J. Y. Cheong, C. Kim, L. Luo, C. Hwang, S. Choi, J. Ryu, S. Kim, W. J. Song, H. K. Song, C. Wang, I. D. Kim, S. Park, Nat. Commun. 10 (2019) 2364.

[57] C. Niu, J. Meng, X. Wang, C. Han, M. Yan, K. Zhao, X. Xu, W. Ren, Y. Zhao, L. Xu, Q. Zhang, D. Zhao, L. Mai, Nat. Commun. 6 (2015) 7402.

[58] X. Li, W. Chen, Q. Qian, H. Huang, Y. Chen, Z. Wang, Q. Chen, J. Yang, J. Li, Y. W. Mai, Adv. Energy Mater. (2020) 2000845. https://doi.org/10.1002/aenm.202000845.

[59] T. Lei, W. Chen, Y. Hu, W. Lv, X. Lv, Y. Yan, J. Huang, Y. Jiao, J. Chu, C. Yan, C. Wu, Q. Li, W. He, J. Xiong, Adv. Energy Mater. 8 (2018) 1802441.

[60] J.-W. Jung, C.-L. Lee, S. Yu, I.-D. Kim, J. Mater. Chem. A 4 (2016) 703-750.

[61] Y. Liu, N. Zhang, L. Jiao, J. Chen, Adv. Mater. 27 (2015) 6702-6707.

[62] L.-F. Chen, Y. Lu, L. Yu, X. W. Lou, Energy Environ. Sci. 10 (2017) 1777-1783.

[63] J. Wang, Y. Cui, D. Wang, Adv. Mater. 31 (2019) 1801993.

[64] J. Nai, X. W. D. Lou, Adv. Mater. 31 (2019) 1706825.

[65] Y. Fang, X.-Y. Yu, X. W. Lou, Matter 1 (2019) 90-114.

[66] H. Ren, R. Yu, J. Qi, L. Zhang, Q. Jin, D. Wang, Adv. Mater. 31 (2019) 1805754.

[67] C. Guan, X. Liu, W. Ren, X. Li, C. Cheng, J. Wang, Adv. Energy Mater. 7 (2017) 1602391.

[68] Y. Fang, X. Y. Yu, X. W. D. Lou, Angew. Chem. Int. Ed. 58 (2019) 7744-7748.

[69] L. Yu, H. B. Wu, X. W. D. Lou, Accounts Chem. Res. 50 (2017) 293-301.

[70] J. Feng, Y. Yin, Adv. Mater. 31 (2019) 1802349.

[71] M. Yan, P. He, Y. Chen, S. Wang, Q. Wei, K. Zhao, X. Xu, Q. An, Y. Shuang, Y. Shao, K. T. Mueller, L. Mai, J. Liu, J. Yang, Adv. Mater. 30 (2018) 1703725.

[72] F. Wan, L. Zhang, X. Dai, X. Wang, Z. Niu, J. Chen, Nat. Commun. 9 (2018) 1656.

[73] L. Ma, N. Li, C. Long, B. Dong, D. Fang, Z. Liu, Y. Zhao, X. Li, J. Fan, S. Chen, S. Zhang, C. Zhi, Adv. Funct. Mater. 29 (2019) 1906142.

[74] M. Liao, J. Wang, L. Ye, H. Sun, Y. Wen, C. Wang, X. Sun, B. Wang, H. Peng, Angew. Chem. Int. Ed. 59 (2020) 2273-2278.

[75] J. Ding, Z. Du, L. Gu, B. Li, L. Wang, S. Wang, Y. Gong, S. Yang, Adv. Mater. 30 (2018) 1800762.

[76] M. Huang, J. Meng, Z. Huang, X. Wang, L. Mai, J. Mater. Chem. A 8 (2020) 6631-6637.

[77] M. Huang, X. Wang, J. Meng, X. Liu, X. Yao, Z. Liu, L. Mai, Nano Energy 77 (2020) 105069.

[78] M. Qin, W. Ren, J. Meng, X. Wang, X. Yao, Y. Ke, Q. Li, L. Mai, ACS Sustain. Chem. Eng. 7 (2019) 11564-11570.

[79] B. He, P. Man, Q. Zhang, C. Wang, Z. Zhou, C. Li, L. Wei, Y. Yao, Small 15 (2019) 1905115.

[80] R. Li, Y. Wang, C. Zhou, C. Wang, X. Ba, Y. Li, X. Huang, J. Liu, Adv. Funct. Mater. 25 (2015) 5384-5394.

[81] C. Guan, W. Zhao, Y. Hu, Q. Ke, X. Li, H. Zhang, J. Wang, Adv. Energy Mater. 6 (2016) 1601034.

[82] P. Yang, Y. Ding, Z. Lin, Z. Chen, Y. Li, P. Qiang, M. Ebrahimi, W. Mai, C. P. Wong, Z. L. Wang, Nano Lett. 14 (2014) 731-736.

[83] X. Lu, M. Yu, T. Zhai, G. Wang, S. Xie, T. Liu, C. Liang, Y. Tong, Y. Li, Nano Lett. 13 (2013) 2628-2633.

[84] M. Li, J. Meng, Q. Li, M. Huang, X. Liu, K. A. Owusu, Z. Liu, L. Mai, Adv. Funct. Mater. 28 (2018) 1802016.

[85] Y. Zeng, Y. Meng, Z. Lai, X. Zhang, M. Yu, P. Fang, M. Wu, Y. Tong, X. Lu, Adv. Mater. 29 (2017) 1702698.

Figs Captions

Fig. 1 (a) Graphic representation of the NTP crystal structure. (b) SEM image, (c) TEM image, (d) elemental mapping analysis of Na, Ti, P, and O, (e) EDS spectrum (Inset is the atomic percentage), (f) high-resolution TEM image, (g) the corresponding SAED pattern, and (h) XRD pattern of HNTP. (i) Nitrogen adsorption-desorption isotherms of HNTP and SNTP.

Fig. 2 (a) Schematic fabrication process of HNTP@PNC film. (b-c) Morphological analysis carried out with SEM, (d) Morphological analysis carried out with TEM (e), Morphological analysis carried out with high-resolution TEM, and (f) elemental mapping analysis of C, N, O, Na, Ti, and P of HNTP@PNC film.

Fig. 3 (a) XRD pattern and (b) Raman spectrum of HNTP@PNC film. (c) TG curves of HNTP and HNTP@PNC film. X-ray photoelectron spectroscopy (XPS) spectra of (d) Na 1s, (e) Ti 2p, (f) P 2p, (g) O 1s, (h) C 1s, and (i) N 1s for HNTP@PNC film.

Fig. 4 (a) Cyclic voltammetry (CV) curves comparison at 5 mV s^{-1} of PNC film and HNTP@PNC film. Comparative (b) galvanostatic charge-discharge (GCD curves) at 1.10 A g^{-1} and (c) Nyquist plots of SNTP@PNC film and HNTP@PNC film. (d) Cyclic voltammetry (CV) curves at various scan rates, (e) the corresponding b values, and (f) GCD curves at various current densities of HNTP@PNC film. (g) Rate capability at various current densities from 0.275 to 5.50 A g^{-1}, (h) long-term cycling performance with the corresponding Coulombic efficiency at 5.50 A g^{-1} of HNTP@PNC film.

Fig. 5 Theoretical investigations of NTP@NC: Optimized structure of NTP@NC form the (a) side and (b) top view; (c) Calculated density of states of NTP and NTP@NC; (d) Formation energy of Na intercalations into NTP to form NxTP (x=1, 2, 3, and 4); (e) Diffusion barriers of

Na ions through NC sheets with 1-3 vacancy defects; (f) Diffusion barriers of Na ions along three diffusion paths for the NTP bulk, NTP surface and NTP@NC interface. Inset illustrates the M1 and M2 occupation sites of Na, as well as the three diffusion paths.

Fig. 6 (a) Schematic diagram of flexible quasi-solid-state ARSIBs with a sandwiched structure. (b) Schematic illustration of reversible Na^+ intercalation/deintercalation during charge/discharge process for HNTP//KZHCF ARSIB. (c) CV curves of HNTP@PNC anode and CNT@KZHCF cathode in the 1 M $NaClO_4$ aqueous electrolyte at 5 mV s^{-1}. (d) CV curves of our ARSIB at various scan rates. (e) Capacitive (red) and diffusion-controlled contribution to charge storage at 5 mV s^{-1} for our flexible battery. (f) Capacitive and diffusion-controlled capacities for the ARSIB at various scan rates. (g) GCD curve of the assembled flexible ARSIB at various current densities. (h) Volumetric energy and power densities of the assembled device compared with previously reported flexible aqueous energy-storage devices. (i) GCD curves of our device under different bending angles from 0^o to 180^o.

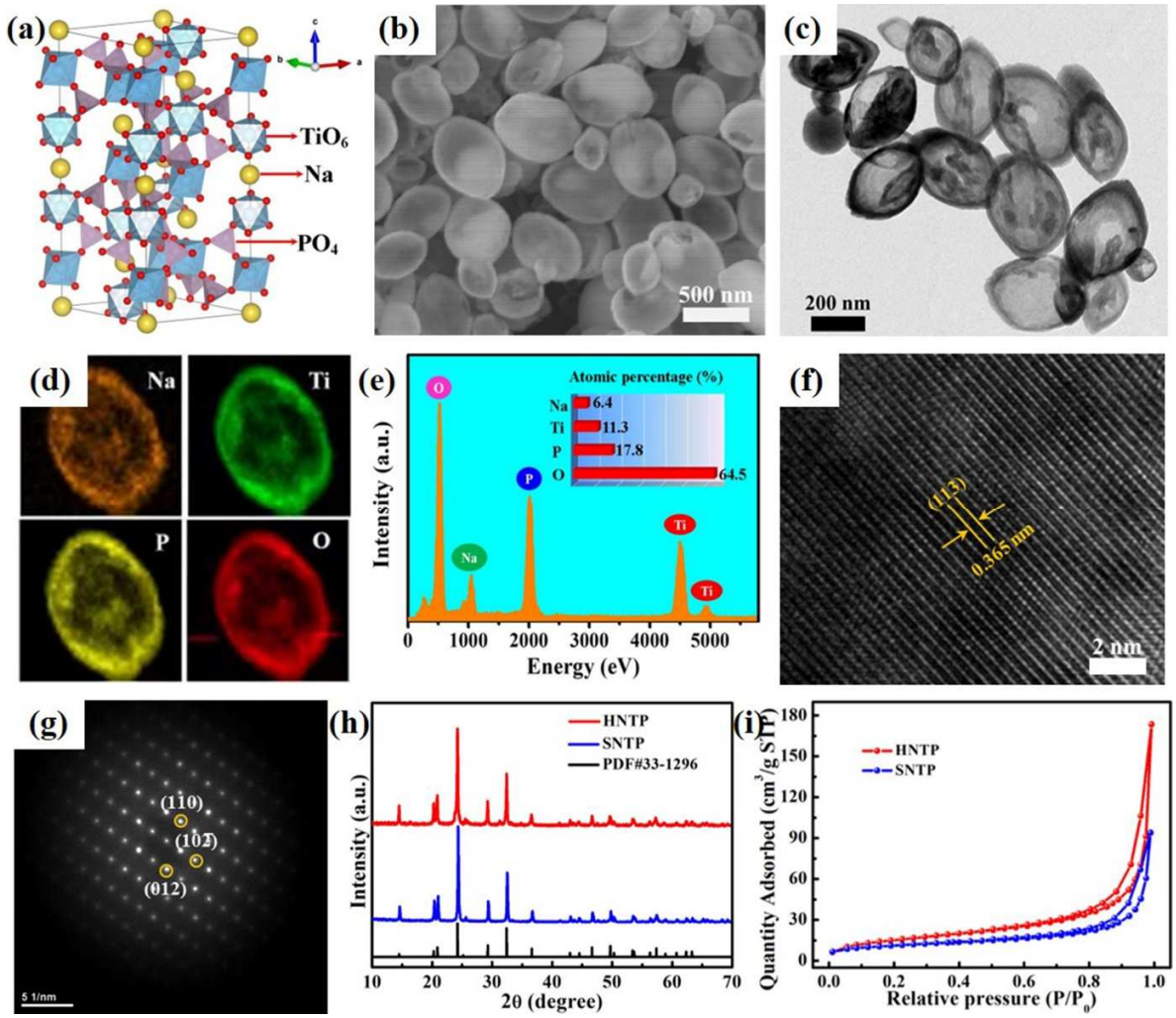

Fig. 1. (a) Graphic representation of the NTP crystal structure. (b) SEM image, (c) TEM image, (d) elemental mapping analysis of Na, Ti, P, and O, (e) EDS spectrum (Inset is the atomic percentage), (f) high-resolution TEM image, (g) the corresponding SAED pattern, and (h) XRD pattern of HNTP. (i) Nitrogen adsorption-desorption isotherms of HNTP and SNTP.

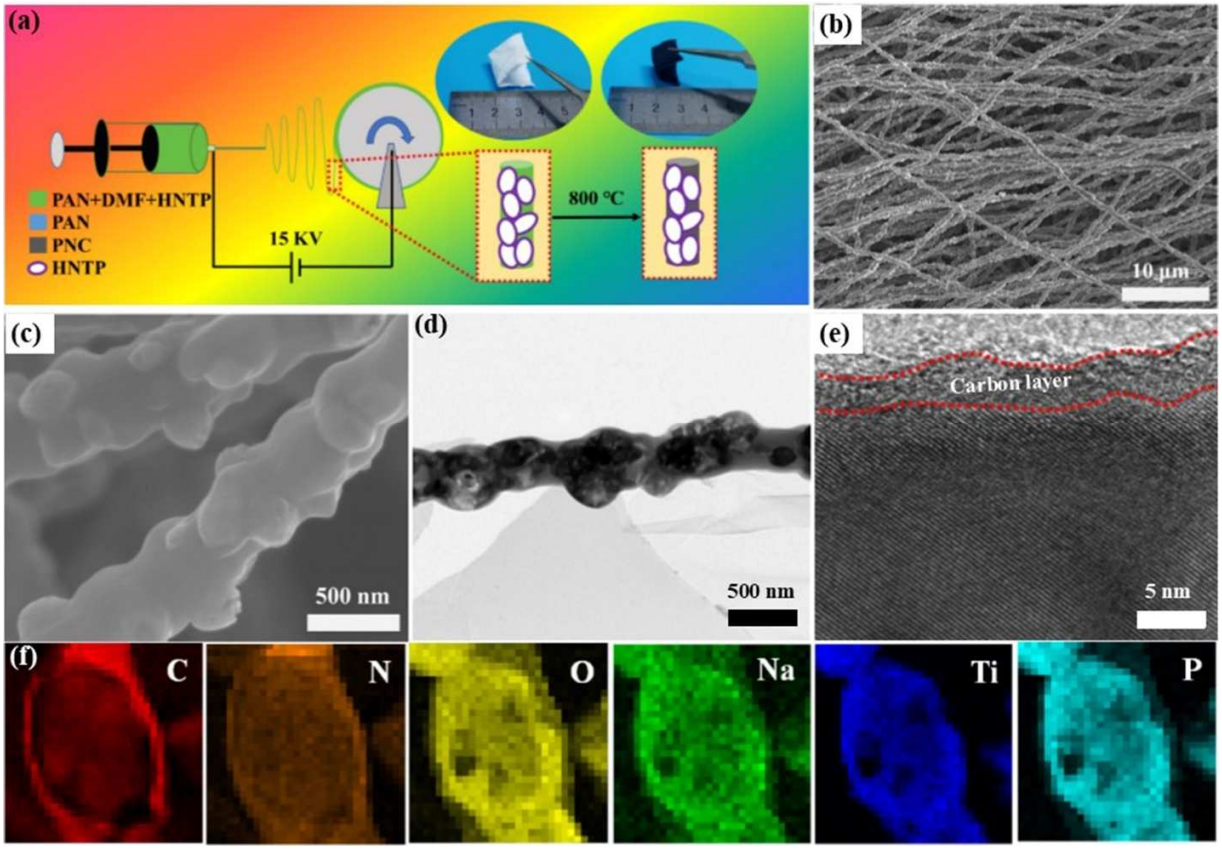

Fig. 2. (a) Schematic fabrication process of HNTP@PNC film. (b-c) Morphological analysis carried out with SEM, (d) Morphological analysis carried out with TEM (e), Morphological analysis carried out with high-resolution TEM, and (f) elemental mapping analysis of C, N, O, Na, Ti, and P of HNTP@PNC film.

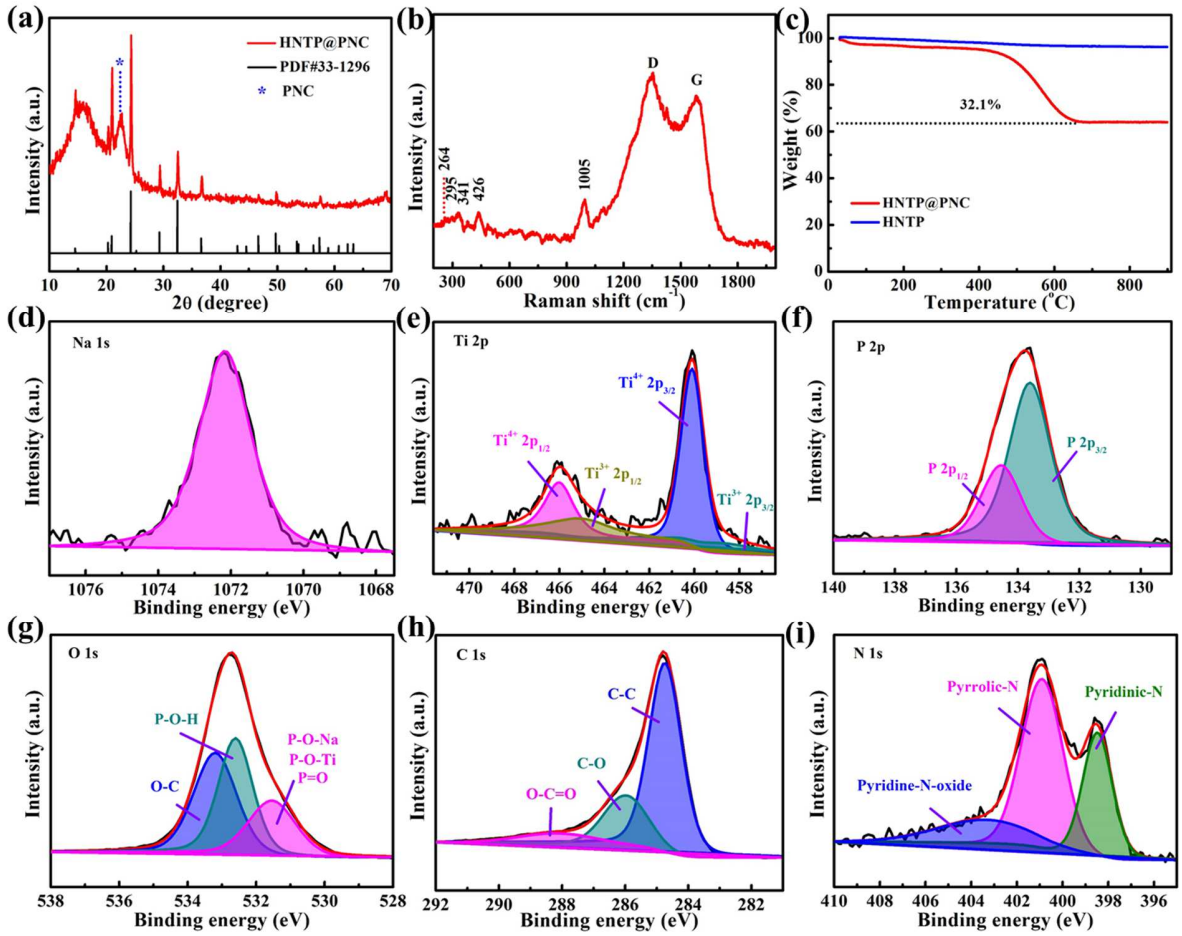

Fig. 3. (a) XRD pattern and (b) Raman spectrum of HNTP@PNC film. (c) TG curves of HNTP and HNTP@PNC film. X-ray photoelectron spectroscopy (XPS) spectra of (d) Na 1s, (e) Ti 2p, (f) P 2p, (g) O 1s, (h) C 1s, and (i) N 1s for HNTP@PNC film.

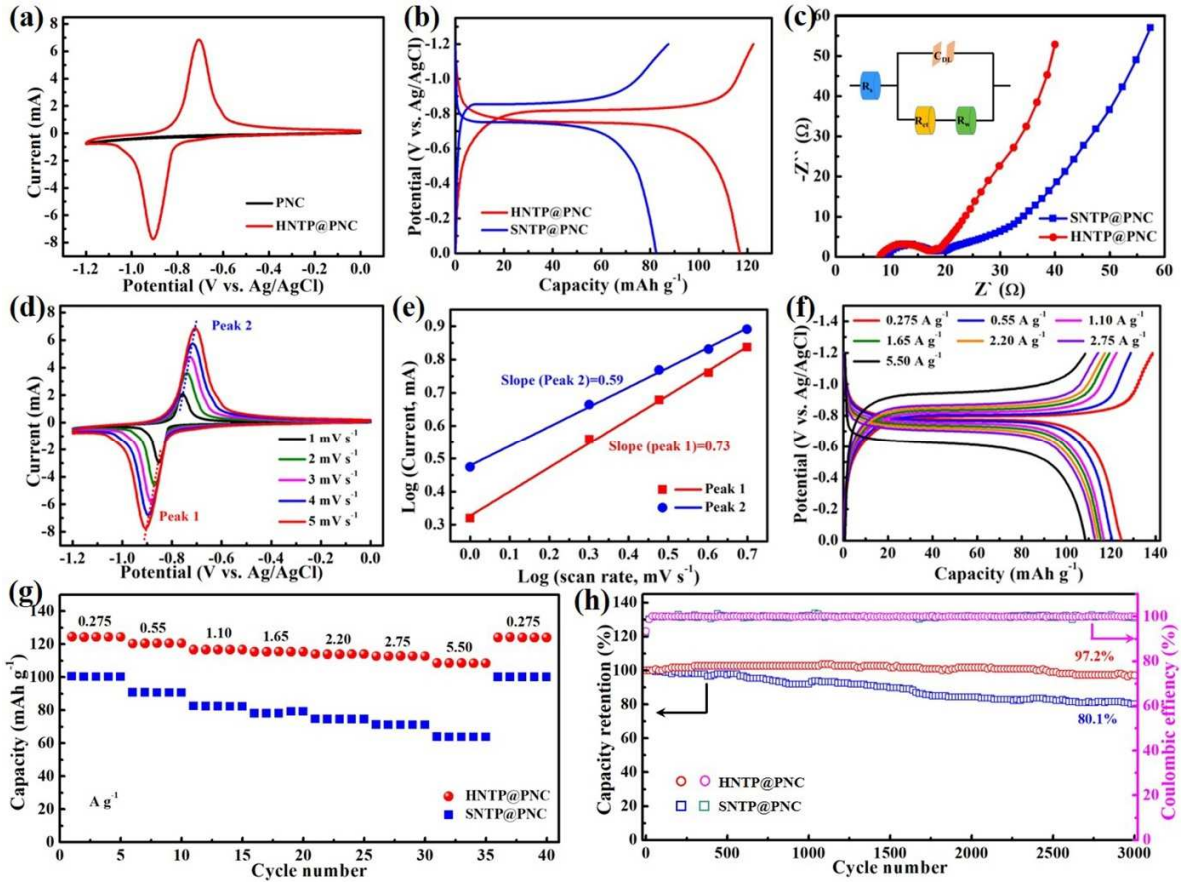

Fig. 4. (a) Cyclic voltammetry (CV) curves comparison at 5 mV s^{-1} of PNC film and HNTP@PNC film. Comparative (b) galvanostatic charge-discharge (GCD curves) at 1.10 A g^{-1} and (c) Nyquist plots of SNTP@PNC film and HNTP@PNC film. (d) Cyclic voltammetry (CV) curves at various scan rates, (e) the corresponding b values, and (f) GCD curves at various current densities of HNTP@PNC film. (g) Rate capability at various current densities from 0.275 to 5.50 A g^{-1}, (h) long-term cycling performance with the corresponding Coulombic efficiency at 5.50 A g^{-1} of HNTP@PNC film.

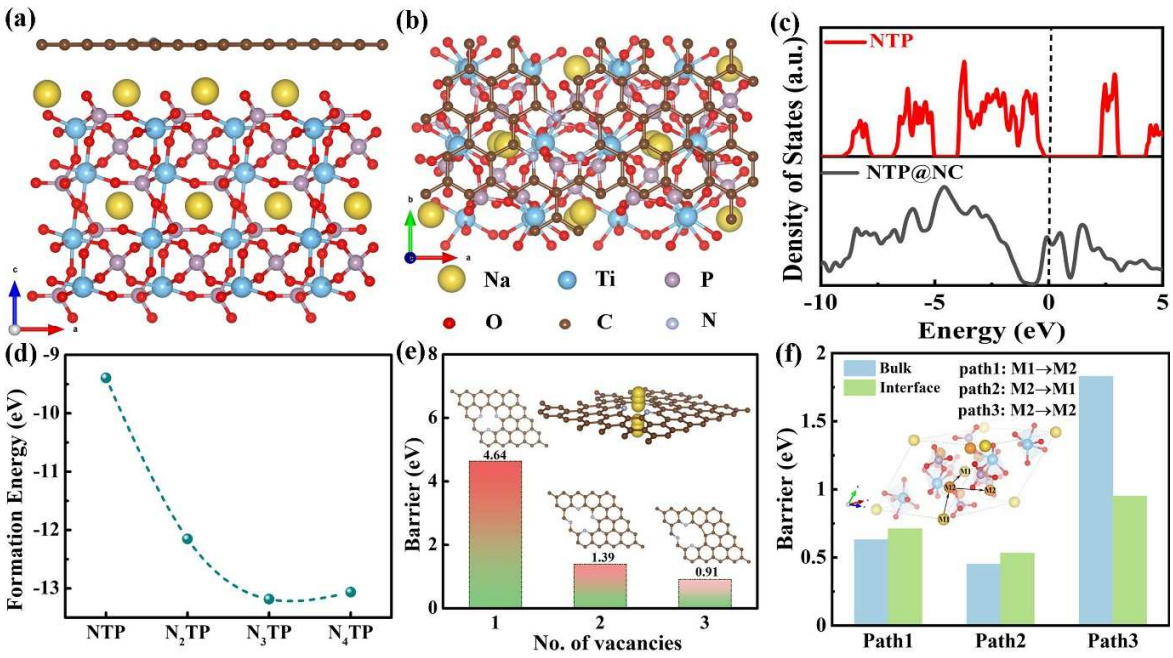

Fig. 5. Theoretical investigations of NTP@NC: Optimized structure of NTP@NC form the (a) side and (b) top view; (c) Calculated density of states of NTP and NTP@NC; (d) Formation energy of Na intercalations into NTP to form NxTP (x=1, 2, 3, and 4); (e) Diffusion barriers of Na ions through NC sheets with 1-3 vacancy defects; (f) Diffusion barriers of Na ions along three diffusion paths for the NTP bulk, NTP surface and NTP@NC interface. Inset illustrates the M1 and M2 occupation sites of Na, as well as the three diffusion paths.

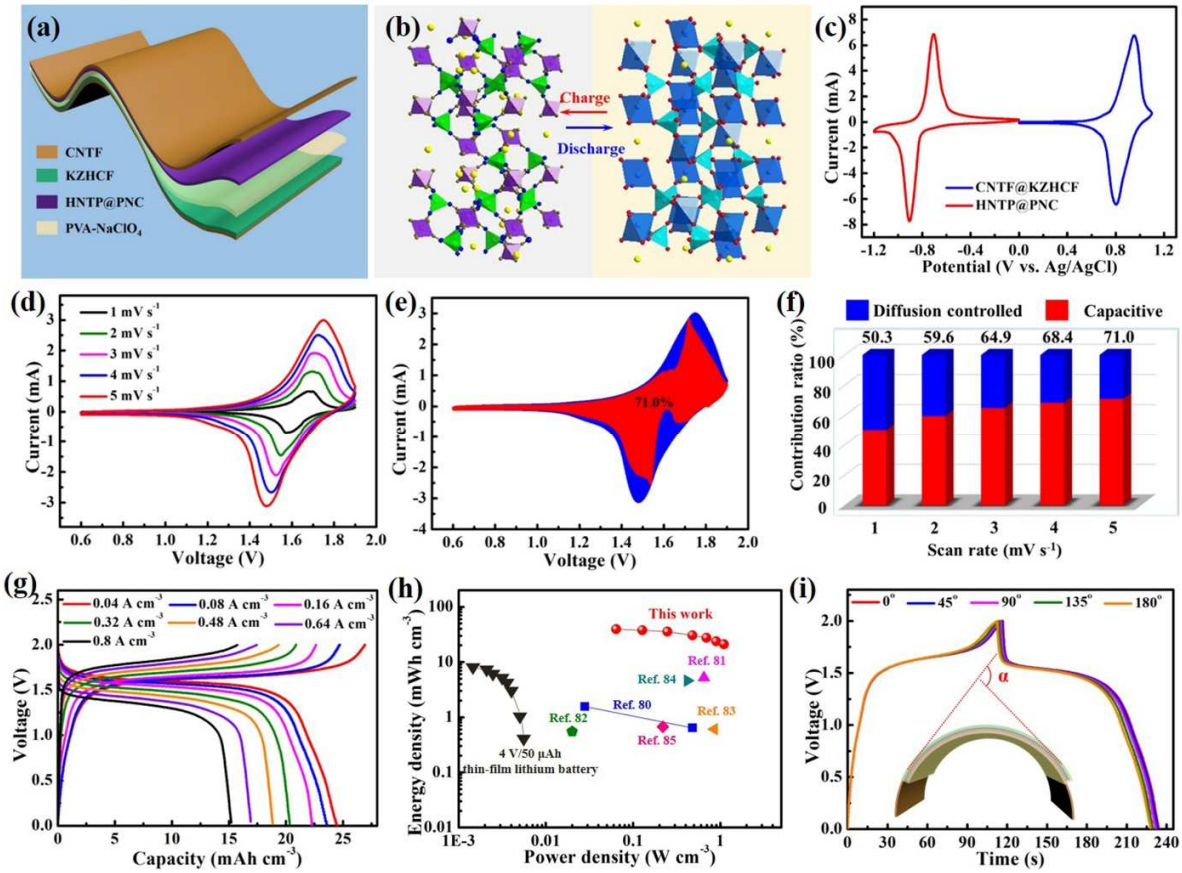

Fig. 6. (a) Schematic diagram of flexible quasi-solid-state ARSIBs with a sandwiched structure. (b) Schematic illustration of reversible Na^+ intercalation/deintercalation during charge/discharge process for HNTP//KZHCF ARSIB. (c) CV curves of HNTP@PNC anode and CNTF@KZHCF cathode in the 1 M $NaClO_4$ aqueous electrolyte at 5 mV s^{-1}. (d) CV curves of our ARSIB at various scan rates. (e) Capacitive (red) and diffusion-controlled contribution to charge storage at 5 mV s^{-1} for our flexible battery. (f) Capacitive and diffusion-controlled capacities for the ARSIB at various scan rates. (g) GCD curve of the assembled flexible ARSIB at various current densities. (h) Volumetric energy and power densities of the assembled device compared with previously reported flexible aqueous energy-storage devices. (i) GCD curves of our device under different bending angles from 0° to 180°.

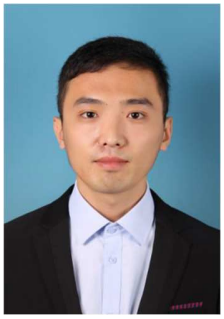

Dr. Bing He received his M.S. degree (2017) from China University of Petroleum. He received his Ph.D. degree (2020) from University of Science and Technology of China. He is currently a Research Fellow in Prof. Lei Wei's research group in the School of Electrical and Electronic Engineering, Nanyang Technological University. His research is focusing on flexible aqueous rechargeable sodium-ion batteries.

Dr. Kuibo Yin is currently an Associate Professor at Southeast University, Nanjing, China. He received his Ph.D. in Materials Science from Nanjing University in 2008. His research interests focus on the characterization and application of energy storage materials and novel 2D materials. He has authored more than 90 SCI journal papers with total citation times more than 4500 and has filed over dozen patents.

Dr. Wenbin Gong is an associate professor in Xuzhou University of Technology. He received his Ph.D. degree in 2014 from Shanghai Institute of Applied Physics, Chinese Academy of Sciences, and then worked as a postdoctoral fellow in Suzhou Institute of Nano-Tech and Nano-Bionics, Chinese Academy of Sciences. His current research interests mainly focus on the simulations of electrocatalysis, electrical and mechanical properties of nano-materials.

Yuwei Xiong is currently an assistant engineer at Key Laboratory of MEMS of the Ministry of Education, Southeast University, Nanjing. She received her master's degree in Electronic Science and Engineering from Southeast University in 2019. Her research interests involve the in situ experimentation inside the electron microscope and applications of nanomaterials in electromechanical systems.

Dr. Qichong Zhang received his B.S. degree in 2013 from Shanghai Institute of Technology, China. He was doing his research work in Suzhou Institute of Nano-Tech and Nano-Bionics as an exchange student from 2015 to 2018. He received his Ph.D. degree (2017) in Condensed Matter Physics from Tongji University. He is currently a Research Fellow in Prof. Lei Wei's research group in the School of Electrical and Electronic Engineering, Nanyang Technological University. His current research interests focus on synthesis of aqueous electrochemical nanomaterials andfiber-shaped functional device design.

Jiao Yang received the B.E. degree in Material Forming and Controlling Engineering from Harbin Institute of Technology in 2015 and then received the M.S. degree in Precision Engineering from Nanyang Technological University in 2016. Now she is a Ph.D. candidate in the school of Electrical and Electronic Engineering in Nanyang Technological University. Her main research interests are aqueous energy storage device.

Zhixun Wang received his B.S. (2013) and M.S. (2016) in Materials Science and Engineering from Central South University. He is now a Ph.D. candidate in School of Electrical and Electronic Engineering at Nanyang Technological University. His research interests lie in the area of multi-material multi-functional fibres.

Zhe Wang received B.S. (2013) in Functional Materials and M.S. (2016) in Material Physics and Chemistry from Lanzhou University. Now he is a Ph.D. student in School of Electrical and Electronic Engineering at Nanyang Technological University. His research mainly focuses on fiber-based devices.

Dr. Mengxiao Chen received her B.S. degree in physics (2012) from Northeastern University and Ph. D. in physics (2017) from Beijing Institute of Nanoenergy and Nanosystems, CAS, China. She is currently a research fellow in Prof. Wei Lei's group in Nanyang Technological University. Her main research interests are novel self-powered systems and multifunctional electric and photoelectric devices and is now focusing on soft material-based devices and their applications.

Ping Man received her B.S. degree from Shandong Agricultural University in 2017, and obtained her M.S. degree from Suzhou Institute of Nano-Tech and Nano-Bionics, China University of Science and Technology under the guidance of Prof. Yagang Yao in 2020. She is currently a PhD candidate in Dr. Thuc Hue Ly's group in City University of Hong Kong. Her research interests include energy storage materials and one-chip electrochemistry.

Dr. Philippe Coquet is affiliated to School of Electrical & Electronic Engineering, Nanyang Technological University as a Visiting Professor. His contributions have acclaimed recognition from honourable subject experts around the world. He is actively associated with different societies and academies. His academic career is decorated with several reputed awards and funding. His research interests include Millimeter wave antennas, Flexible electronic, RF MEMS, Nanotechnology for RF, Microfluidic

Dr. Yagang Yao received the B.S. degree in chemistry fromLanzhou University, Lanzhou in 2004, and the Ph.D. degree in physical chemistry from Peking University in 2009. He was a Post-Doctoral Fellow with the Materials Science and Engineering Department, Georgia Institute of Technology, Atlanta, GA, USA, from 2009 to 2013. Then he joined the Suzhou Institute of Nano-Tech and Nano-Bionics, Chinese Academy of Science as a Professor from 2014 to 2018. He is currently a full Professor with the College of Engineering and Applied Sciences, Nanjing University. His current research interest focusses on next-generation electrode materials in energy storage systems.

Dr. Litao Sun is currently a Distinguished Professor at Southeast University, Nanjing, China. He received his Ph.D. from the Shanghai Institute of Applied Physics, Chinese Academy of Sciences, followed by postdoctoral research at University of Mainz, Germany and a visiting professorship at the University of Strasbourg, France. His current research interests include in situ experimentation inside the electron microscope, graphene and related 2D materials, new phenomena from sub-10 nm nanoparticles, and applications of nanomaterials in environment, energy, and nanoelectromechanical systems.

Dr. Lei Wei received the B.E. degree in Electrical Engineering from Wuhan University of Technology in 2005; and the Ph.D. degree in Photonics Engineering from Technical University of Denmark in 2010. Then he joined the Research Laboratory of Electronics at the Massachusetts Institute of Technology as a postdoctoral associate. In September 2014, he joined the School of Electrical and Electronic Engineering at Nanyang Technological University in Singapore as a Nanyang Assistant Professor. In August 2019, he was promoted to Associate Professor. His main research interests are fiber-based optoelectronic devices, novel multi-functional fiber structures, bio-fiber interfaces, and in-fiber energy generation and storage.

Graphical Abstract